


RESEARCH ARTICLE

Magnetic resonance imaging as a tool for quality control in extrusion-based bioprinting

Barbara Schmieg^{1,2}  | Sarah Gretzinger^{1,2} | Sebastian Schuhmann³ |
Gisela Guthausen^{3,4} | Jürgen Hubbuch^{1,2}

¹Institute of Functional Interfaces, Karlsruhe Institute of Technology (KIT), Karlsruhe, Germany

²Institute of Engineering in Life Sciences, Section IV: Molecular Separation Engineering, Karlsruhe Institute of Technology (KIT), Karlsruhe, Germany

³Institute of Mechanical Process Engineering and Mechanics, Karlsruhe Institute of Technology (KIT), Karlsruhe, Germany

⁴Engler Bunte Institute Water Chemistry and Technology, Karlsruhe Institute of Technology (KIT), Karlsruhe, Germany

Correspondence

Jürgen Hubbuch, Institute of Engineering in Life Sciences, Section IV: Biomolecular Separation Engineering, Karlsruhe Institute of Technology (KIT), Fritz-Haber-Weg 2, 76131 Karlsruhe, Germany.
Email: juergen.hubbuch@kit.edu

Funding information

German Federal Ministry of Education and Research

Abstract

Bioprinting is gaining importance for the manufacturing of tailor-made hydrogel scaffolds in tissue engineering, pharmaceutical research and cell therapy. However, structure fidelity and geometric deviations of printed objects heavily influence mass transport and process reproducibility. Fast, three-dimensional and nondestructive quality control methods will be decisive for the approval in larger studies or industry. Magnetic resonance imaging (MRI) meets these requirements for characterizing heterogeneous soft materials with different properties. Complementary to the idea of decentralized 3D printing, magnetic resonance tomography is common in medicine, and image data processing tools can be transferred system-independently. In this study, a MRI measurement and image analysis protocol was evaluated to jointly assess the reproducibility of three different hydrogels and a reference material. Critical parameters for object quality, namely porosity, hole areas and deviations along the height of the scaffolds are discussed. Geometric deviations could be correlated to specific process parameters, anomalies of the ink or changes of ambient conditions. This strategy allows the systematic investigation of complex 3D objects as well as an implementation as a process control tool. Combined with the monitoring of metadata this approach might pave the way for future industrial applications of 3D printing in the field of biopharmaceutics.

KEYWORDS

bioprinting, image analysis, magnetic resonance imaging (MRI), quality control, reproducibility

1 | INTRODUCTION

Achieving a high degree of individualization while keeping production time and costs low are among the critical challenges for the entry to

the market of personalized medical devices and therapies. 3D printing is one manufacturing method that may meet these demands in terms of fast automated production of individual objects.^[1] The span of suitable materials ranges from metal or thermoplastics for mechanically strained medical aids to soft biomaterials for tissue engineering.^[2–5] Hereby, cells are incorporated within hydrogels, creating an artificial scaffold that will induce the growth of new tissue upon healing.

A reliable and reproducible product quality will be decisive for the industrial application, especially in the medical context^[6] or for the

Abbreviations: BX, BioX (Cellink) bioprinter; CT, computed tomography; GelMA, gelatin-based bioink functionalized with methacryloyl groups; H_i, Kruskal–Wallis H value of group i; MRI, magnetic resonance imaging; MRT, magnetic resonance tomography; p, probability value; PLA, polylactic acid; RARE, rapid acquisition with relaxation enhancement; RH, 3DDiscovery (regenHU) bioprinter; μ CT, micro computed tomography

This is an open access article under the terms of the Creative Commons Attribution-NonCommercial License, which permits use, distribution and reproduction in any medium, provided the original work is properly cited and is not used for commercial purposes.

© 2022 The Authors. *Biotechnology Journal* published by Wiley-VCH GmbH

application in high throughput 3D assays.^[7,8] To ensure this, two main control strategies are available.

The first approach is the in-process monitoring of the 3D printing procedure based on optical methods.^[9–11] Similar process optimization strategies include the preceding image-analysis of larger datasets of printed objects to define the acceptable parameter range. Among the important parameters are thickness and uniformity,^[12,13] the structure fidelity of extruded filaments while traversing lower orthogonal layers^[14] and the connectivity respectively the separation of channels or pore systems.^[15]

The second control strategy is to ensure the quality of the individual 3D printed object in a nondestructive manner. As scaffolds are tailor-made from an often-limited stock of biological material, sampling on a random basis is not possible. The analytical procedure must be performed fast, without toxic or radioactive contrast agents and in 3D to capture defects within the objects before applying it to a patient. Different optical approaches with medical or process engineering backgrounds have already been proposed. Up to now, application examples are predominantly shown for opaque, solid parts intended for short-time use e.g. cutting guides or drill templates for implant placement or imaging phantoms.^[16–18] Compared to that, characterizing glossy hydrogels that lack transport stability and are prone to degradation is more challenging.

Reasons for that might be found in the intrinsic limitations of conventional analytic strategies when it comes to reflective gel materials. For optical microscopy, parameters like resolution, penetration depth and field of view depend on the instrument type.^[19] This is critical in the case of bioprinted scaffolds, where macroscopic scaffold structure fidelity and aspects on a smaller scale, for example internal porosity, are of interest.^[20,21] Long analysis durations caused by image stitching as well as sample drying, reflective surfaces and nonideal temperature gradients narrow the applicability.^[22–24] For the application of white-light interferometry, similar challenges exist.^[23]

3D imaging techniques like computed tomography (CT) or MRI (magnetic resonance imaging, in medical context magnetic resonance tomography, MRT) offer a high measurement depth for monitoring hydrated, large objects at ambient conditions. They are not commonly used for quality control in 3D printing yet, as the availability of these methods is limited by the high initial cost and complexity of operation. The potential for the application on hydrogels lies in the contrast generation without the use of any toxic contrast agents, unlike another medical imaging technique as the positron emission tomography.^[25,26] The achievable resolution in both techniques, CT and MRT and their pendants in material science μ CT and MRI, is a compromise between short analysis time with low impact^[27,28] and increasing measurement duration at higher resolution. What discerns MRI from μ CT is the physical principle of contrast generation. The contrast in μ CT images mainly depends on the atomic number and the density of the material. Both are low for soft tissues. Increasing it with higher impact measurements might dry the hydrogel. Contrast in ^1H -MRI, on the other hand, is given by the ^1H -spin density and substance-specific relaxation times, which means that good soft tissue contrasts can be achieved.^[29] Materials for bioprinting are developed to mimic natural soft tissues and bones.

The application of MRI on these hydrogels in this manuscript proposes a future applicability in personalized medicine.

Image analysis provides evidence of typical challenges in bioprinting by analyzing the deviation from the design in actual strand thickness, uniformity and structure fidelity in 3D. Thus, it was applied on MR images, providing a tool for quality control. In this paper, we demonstrate the usefulness of this tool for extrusion-based 3D printing. As a model geometry, a cubic scaffold was chosen. The pattern will give information on the regularity of the extrusion as well as the mass transfer limitations arising from the strand thickness and uniformity. The scaffold total area, porosity and hole size distribution were defined as critical quality attributes. To contribute toward standardization in bioprinting, a dataset of samples produced with three different inks, two extrusion-based 3D printers and a Fused Deposition Modeling reference is analyzed. To establish the method, ink material without cells was used for this study. The inks which are based on alginate, functionalized gelatin and calciumphosphate represent the variability of commonly used materials in literature and their inherent challenges.^[30,31] We will discuss the transferability of materials between printing systems as well as inherent challenges of the hydrogels concerning reproducibility. The aim of controlling the printing process should be to react to deviations in the material like several batches from natural sources, aging material as well as ambient conditions such as temperature or moisture to ensure minimal deviations from the desired geometry.

2 | EXPERIMENTAL SECTION

2.1 | 3D printing

3D printing was executed with two different pneumatic extrusion-based systems ($n_{\text{printer}} = 2$) that were positioned in the same room for comparable ambient conditions (temperature $22^\circ\text{C} \pm 1\text{K}$). The 3DDiscovery (regenHU, Villaz-St-Pierre, Switzerland; abbreviated RH) and the BioX (Cellink AB, Gothenburg, Sweden; BX) were equipped with identical consumables, in detail nozzles (Cellink) and glass slides (Carl Roth, Karlsruhe, Germany). Accordingly, the printing parameters were chosen as similar as possible (see Tables S1 and S2, Supporting Information). The model scaffold (Figure 1) was 3D printed with three different inks ($n_{\text{materials, ink}} = 3$) and a polylactic acid (PLA) reference material ($n_{\text{materials, reference}} = 1$).

The first ink was an alginate – nanocellulose blend that is crosslinked with an aqueous CaCl_2 -solution (Bioink, Cellink) directly after the extrusion process, in the following referred to as “alginate ink.” The crosslinking procedure included the dripping of the liquid over the printed object, its immersion and the removal of residual moisture with a wiping tissue after 20 min of incubation as described by the manufacturer. The material was provided in ready-to-use cartridges (3 ml) and used as received after warming it up to room temperature for 1–2 h, yielding three objects per cartridge ($n_{\text{objects, cartridge}} = 3$).

The thermosensitive GelMA ink (Cellink) was printed at a temperature window of $25.5\text{--}25.8^\circ\text{C}$, set by the cartridge heating systems of the printers. Parameters for the layer-by-layer crosslinking with the

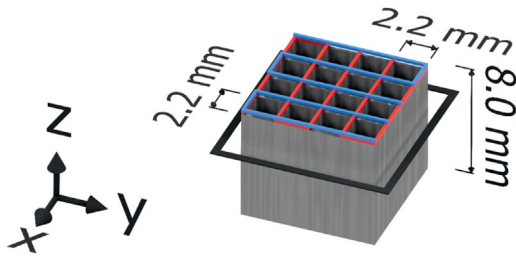


FIGURE 1 Scaffold geometry for the image analysis of 3D printed objects. The designed object consists of meandering lines with a center-to-center distance of 2.2 mm, alternating in a 90° angle between the layers, resulting in a total height of 8 mm (6.5 mm for calciumphosphate). MR imaging is used to monitor 15 axial slices representing 15 xy-cross-sections across the object (details see Chapter 2.2).

365 nm UV-light of the respective printer were 6 s exposure per layer at 30 mm distance. The ready-to-use cartridges (3 ml) were heated to 37°C for 30 min in a water bath to liquify the gelatin and then positioned in the temperature-controlled printheads for 20 min at the target temperature of 25.5°C before starting the process. The printing process was executed until the cartridges were completely empty, resulting in three or four objects per cartridge ($n_{\text{objects,cartridge}} = 3$ respectively $n_{\text{objects,cartridge}} = 4$).

The calciumphosphate-based Plotter–Paste CPC (Innotere GmbH, Radebeul, Germany) is recommended for research on bone replacement. With its higher solids content, printed geometries are self-supporting. The final mechanical stiffness was achieved by incubating the objects at 100% ambient air moisture and 37°C for 4 days in a cell culture incubator. The ready-to-use material was transferred from a 5 ml to a 3 ml cartridge (Nordsen EFD, Concord, CA, USA) with a Luer–Lock adapter for printing at room temperature with the 3DDiscovery system. The printing process yielded three objects printed from one cartridge ($n_{\text{cartridge}} = 1$, $n_{\text{objects,cartridge}} = 3$). As reference objects, polylactic acid (PLA) scaffolds ($n_{\text{objects}} = 3$) were additionally produced with an i3 MK3 fused deposition modeling printing system (Prusa Research, Prague, Czech Republic).

After the respective postprocessing, all 3D printed objects were stored until MRI measurement for 3–8 days. Hereby, alginate, GelMA and calciumphosphate scaffolds were kept at 5°C in closed 20 ml vials (Carl Roth) under moist conditions, PLA samples at 22°C and ambient air.

2.2 | Magnetic resonance imaging (MRI)

For characterization of the 3D printed objects by MRI, an Avance HD III SWB 200 MHz tomograph (Bruker BioSpin MRI GmbH, Ettlingen, Germany) was used (details see, Table S3, Supporting Information). The imaging gradient unit was thermostated at 20°C, providing a constant environment for the hydrogel. The scaffolds were placed in a 10 ml glass vial with lid (A-Z Analytik-Zubehör GmbH, Langen, Germany) to avoid drying and to facilitate reproducible positioning within the mea-

surement chamber. As background phase for alginate, GelMA and calciumphosphate measurements, air was suited best, whereas PLA reference scaffolds were immersed in a 30% (v/w) ethanol in water solution. The settings are summarized in Table S3, Supporting Information, resulting in a measurement time of 26 min.

A total number of 15 interlaced axial slices, in the following referred to as “cross-sections” of the multislice 2.5D MRI settings, along the z-axis of the object was simultaneously imaged within the specified measurement time and saved in a binary data format. The stacked slices were subsequently transferred into a grayscale matrix. Thus, information on the structure fidelity within 7 mm height of the printed objects were available in the stacked axial slices. In a prescan of the object, the field of view was adapted to the location of the hydrogel in the vial. The position of the bottom slice was chosen manually. Please note that in MRI stacks of 2D images could be measured (i.e., 2.5 D MRI) additionally to the possibility of true 3D images. In the present case 2.5 D MRI was chosen as the measurement time was comparably small to avoid significant drying with its impact on scaffold’s geometry, and the spatial resolution can be chosen sufficiently good.

2.3 | Image analysis

MRI grayscale data were processed in MATLAB (version 2019b, The-MathWorks, Natick, USA) (see Figure 2). Otsu’s threshold^[32] was applied to segment the hydrogel lattice from the background as a pre-processing step. If artifacts due to water droplets or vial edges were present in the picture, the option “imclearborder” was used to remove them before the analysis.

In the case of low contrast between water-filled voids and hydrogel and a failed automatic segmentation, the Image Segmenter App of MATLAB was applied to threshold locally. Within the “Add to mask” option, manually marking background and foreground seed pixels created local binary masks for further processing. Area features were extracted by the summing of pixels in the binary data. In detail, the area of the hydrogel lattice and the respective areas of the holes between the hydrogel strands were quantified for each cross-section. The porosity of a slice was defined as the ratio of all voids to the covered area of lattice and enclosed voids. Hereby, the voids consisted of the holes between the printed strands, water-filled holes and air bubbles within the hydrogel.

2.4 | Statistics

The size of holes within the scaffold area were not normally distributed and contain outliers in the case of noncontinuous hydrogel strands causing larger holes within the scaffold. Furthermore, the number of detected holes varies depending on the ink used. The nonparametric Kruskal–Wallis test followed by a multicomparison (Bonferroni method) in MATLAB was run to evaluate the differences between the groups within an object or between objects. A *p*-value less than 0.05 was considered as statistically significant.

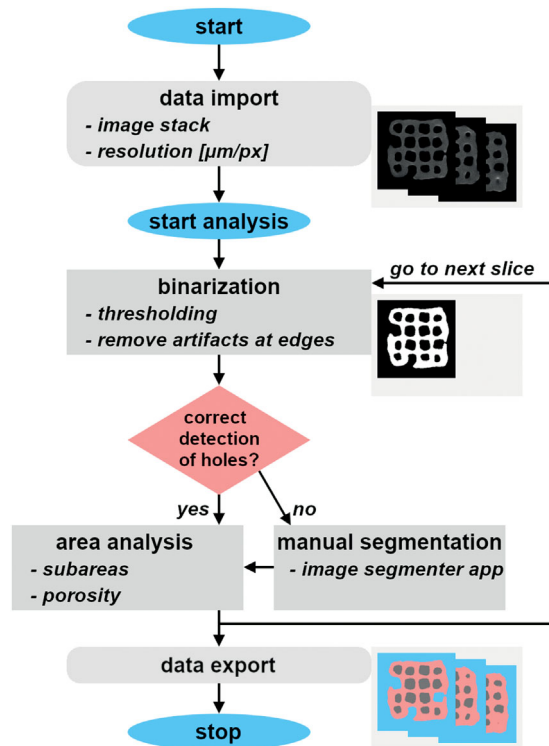


FIGURE 2 Schematic workflow of the image analysis in MATLAB. The imported image data represents 15 cross-sections along the z-axis of a printed object. After image binarization the user is prompted to check the correctness of segmentation into lattice, voids and artifacts. The script returns the key figures related to the slice of the image stack. Exemplary slices visualize the image processing steps.

3 | RESULTS AND DISCUSSION

3.1 | Material printing behavior

Prior to an analysis of the scaffolds, the process variability of the 3D printing process as well as the characteristics of the ink as source of variations need to be considered.

The hydrogel network of the alginate ink (see Figure 3A and B) is fixed by a crosslinking solution that is added on the surface of the object, causing anisotropic swelling (Figure S6, Supporting Information). Swelling influences orthogonality of the object walls as well as the holes, where residual crosslinking solution may remain. Within the data set of 12 objects printed with alginate bioink, 32.5% of the expected holes could be segmented. In three samples less than 13 (of the expected 240) holes accumulated from 15 xy-cross-sections were detectable, indicating a low structure resolution using extrusion-based bioprinting systems.

The viscosity of the GelMA ink is sensitive to changes in temperature as well as the storage time in the cartridge.^[33-35] With the optimal extrusion properties being in the interphase between liquid and gelled state of the ink, the extruded mass flow is sensitive to changes of the ambient conditions. For the application of the scaffolds, differing strand diameters have a huge impact on the scaffold geometry as

well as the diffusive distances in the strands.^[36,37] If uniform extrusion is achieved, the stackability of the ink is high (see Figure 3C and D). To ensure continuous material extrusion two strategies were used for GelMA. In the 3DDiscovery system, temperature settings in the cartridge jacket were maintained throughout the printing process. The piezoelectric heating mantle of the BioX is controlled in an on/off-mode with automatic setting of the upper and lower temperature limit. As the tendency of the ink to clog the nozzle increased at the lower temperature limit, the set temperature was adjusted manually by 0.3 K during the extrusion process in the case of clogging to induce a heating of the system. Furthermore, the gelling delay directly after deposition is influenced by the air temperature within the 3D printer cabinets. During operation, the air temperature around the printing area within the respective cabinet increased with a gradient of about 1°C/h (3DDiscovery) and more than 2°C/h (BioX), which might further influence the structure fidelity of the printed strands.

The calciumphosphate ink is characterized by a high structure fidelity of the extruded strands (Figure 3E and F). The layers remain discernible and do not merge at the crossing points (Figure 3F, arrow). Within the single batch of the calciumphosphate, which was used to print three objects ($n_{\text{objects,cartridge}} = 3$), the reproducibility of the geometry is high compared to the low-viscous alginate and GelMA inks. As a reference for good structure fidelity, PLA filament was extruded ($n_{\text{objects}} = 3$, see Figure 3G and H). The material is mechanically stable, storable and resistant to degradation, swelling, or drying within the spectrometer.

3.2 | Stackability and porosity

For structure fidelity, it is important that the stacked layers of the cube generate orthogonal boundaries, the roughness of the single extruded strand being the only deviation. Figures 4 and 5 show the structure fidelity expressed by the covered area (lattice area and areas of all enclosed voids and air bubbles) and area porosity of the replicates' 15 cross-sections referred to the relative z-height within the object ($n_{\text{slices,object}} = 15$). Hereby, the area porosity of the cross-section is defined as the sum of the voids and air bubbles referred to the covered area. The visualization should ideally result in straight lines of these parameters against the z-height of the object, representing constant properties during the layer-by-layer stacking. The influence of storage time on the objects and the parameters monitored by MRI was analyzed in pretests (see Figure S7, Supporting Information).

The reproducibility of the relevant geometric parameters stacking and porosity of the PLA scaffolds (Figure 4A) were considered as reference ($n_{\text{objects}} = 3$). With regard to the resolution of the applied MRI method (Table S3, Supporting Information), the area of their cross-sections has low deviations at different z-heights of the cube with a mean value of $88.5 \pm 1.4 \text{ mm}^2$ and a range of 10.1 mm^2 , calculated from the 15 stacked slices per object. Furthermore, the porosity is comparable across the total object height (0.48 ± 0.01 , median 0.48, range 0.05). Deviations arise mainly from the layer-by-layer process, which creates a wall roughness and some inconsistencies at the beginning or ending

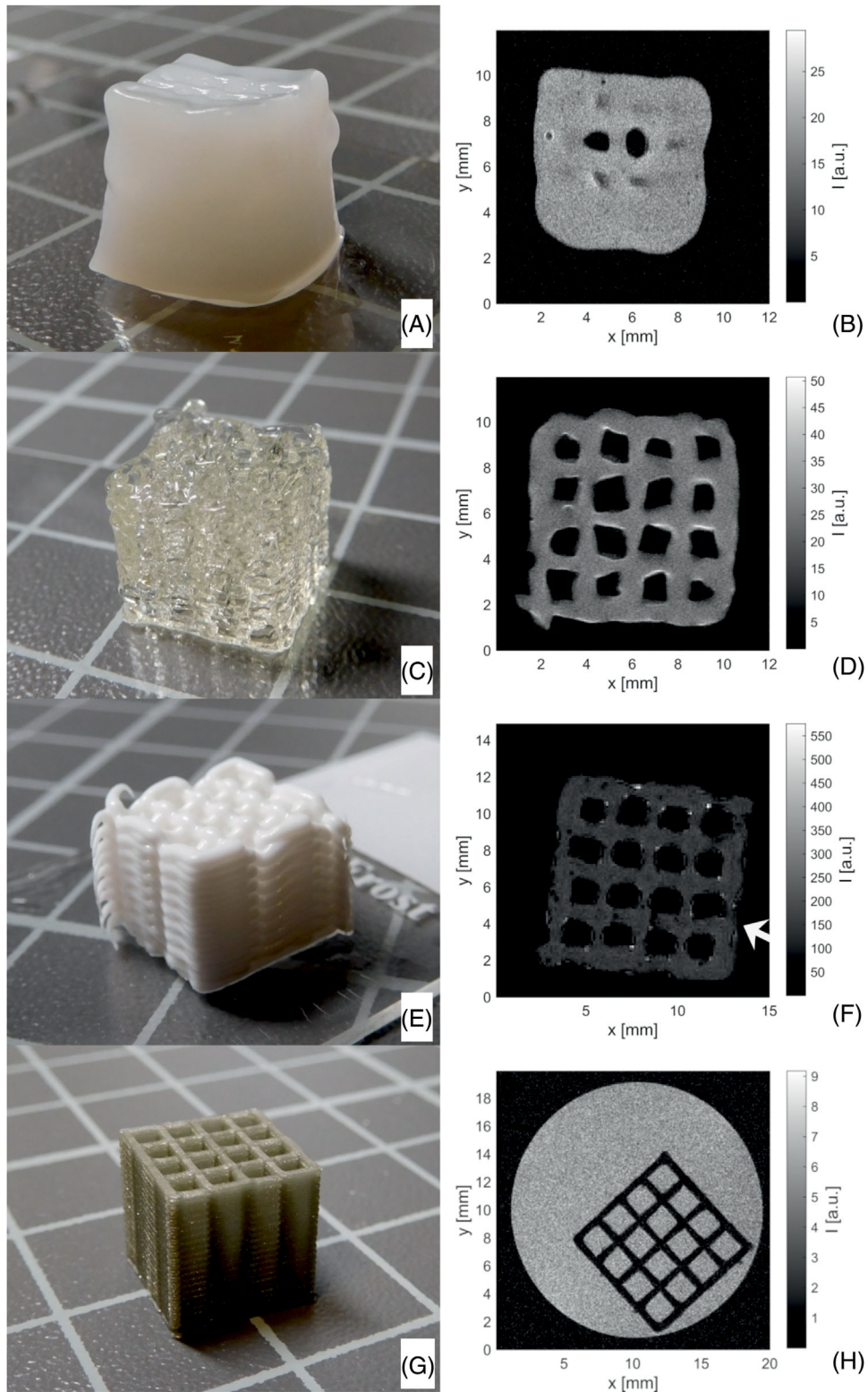


FIGURE 3 Photographs of the alginate (A), GelMA (C), calciumphosphate (E), and PLA (G) scaffolds on a grid of $10 \times 10 \text{ mm}^2$ as well as one representative slice from 2.5 D MRI measurements (B: alginate, D: GelMA, F: calciumphosphate, H: PLA; see Figures S1–S5, Supporting Information, for more information) visualize the dependence of the geometrical features stackability and porosity on the ink.

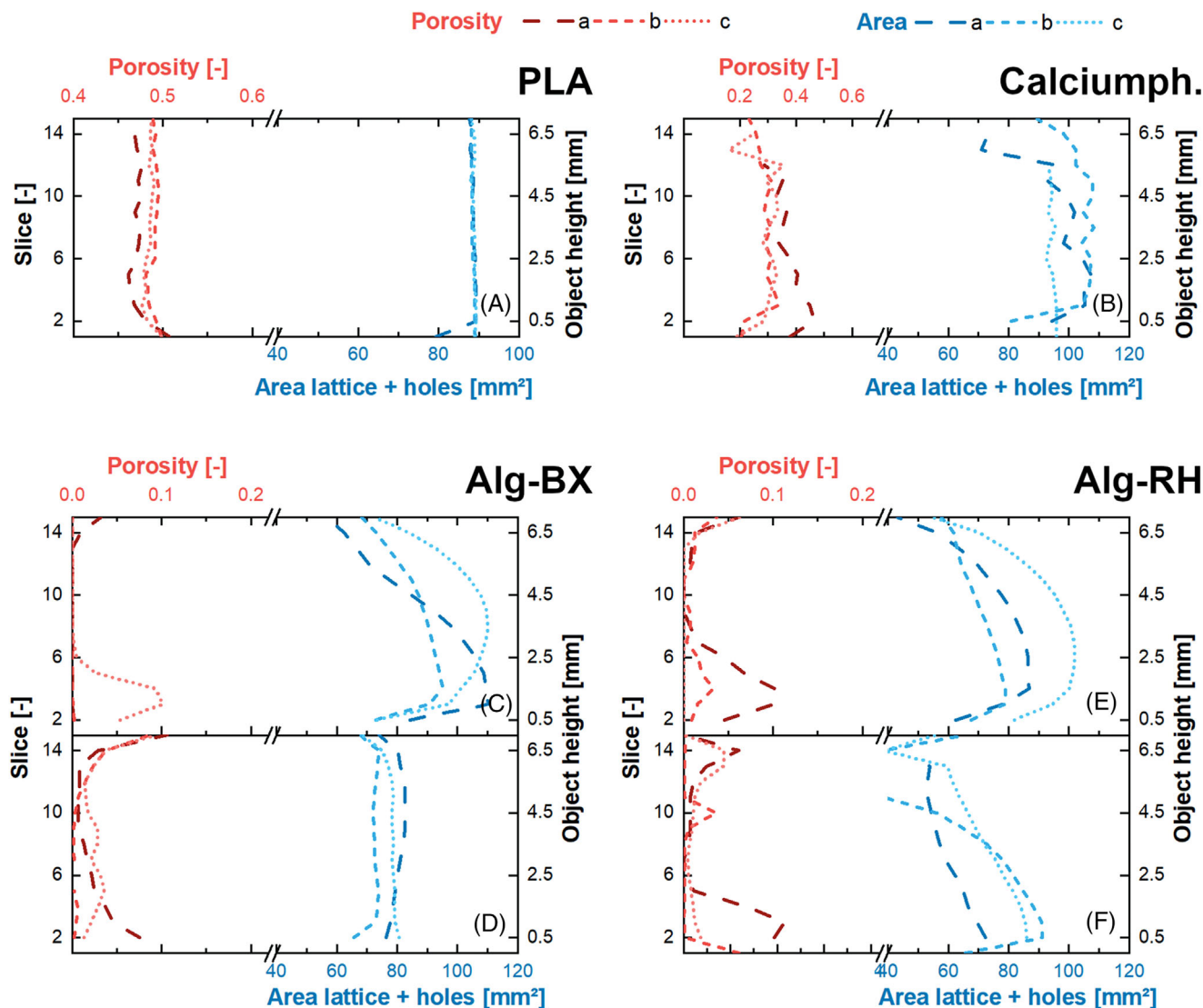


FIGURE 4 Area covered by the hydrogel lattice and its enclosed voids and the resulting porosity of the scaffold displayed against the slice of the 2.5 D MRI data which can be related to a relative object z-height. For each ink cartridge of 3 ml, the letters a-b-c represent the sequence of the objects extruded from one cartridge ($n_{\text{objects,cartridge}} = 3$). A: PLA reference, B calciumphosphate ink, C alginate ink, BioX (BX) printer, batch 1, D alginate, BX, batch 2, E alginate, 3DDiscovery (RH) printer, batch 1, F alginate, RH, batch 2.

of the extruded filament in a specific layer (see Figure S1, Supporting Information, slice 13).

For the three objects printed with calciumphosphate ink ($n_{\text{cartridge}} = 1$, $n_{\text{objects,cartridge}} = 3$, Figure 4B), 40 out of 45 slices were analyzed, yielding a mean porosity of 0.31 ± 0.06 , with a trend of lower porosities as well as a smaller range at increasing object height. Five slices were manually excluded from analysis due to wrap-around artifacts (see Figure S2, Supporting Information, slice 1). The mean covered area of the cross-section (lattice plus enclosed voids and air bubbles) is $96.7 \pm 10.7 \text{ mm}^2$, whereby the deviations are smaller between slices 4 and 12 with a mean area of $100.2 \pm 5.8 \text{ mm}^2$. Deviations are mostly caused by air bubbles within the material and discontinuous strands on the outer edges of the object (see example in Figure S2, Supporting Information), which could be optimized by locally adapting the extrusion velocity or the pre- and post-flow parameters.

In general, the cross-sectional area as well as the porosity of the alginate scaffolds decrease from the bottom to the top of the scaffold in the analyzed dataset of two ink batches ($n_{\text{alginate ink,batch}} = 2$) printed with two printers ($n_{\text{printer}} = 2$) and three objects for each cartridge ($n_{\text{objects,cartridge}} = 3$) ($n_{\text{alginate ink,total}} = 2 \times 2 \times 3 = 12$ objects, Figure 4C–F and *SI Figure 3*). Exceptions are some data points from the lowest slices of the object which have small cross-sectional areas and increased porosity of the topmost slices. Reasons for that might be the anisotropic swelling resulting in a curved bottom area and entrapped water within the scaffold. In the case of applications with diffusive mass transport, local gradients and nutrient limitations at the center of the object will occur.^[38] Concerning the structure fidelity of the layers, a printer-specific behavior and a difference between ink batches was observed. With the BioX system, the strands tended to merge to a higher degree, resulting in a lower porosity of 0.02 ± 0.03

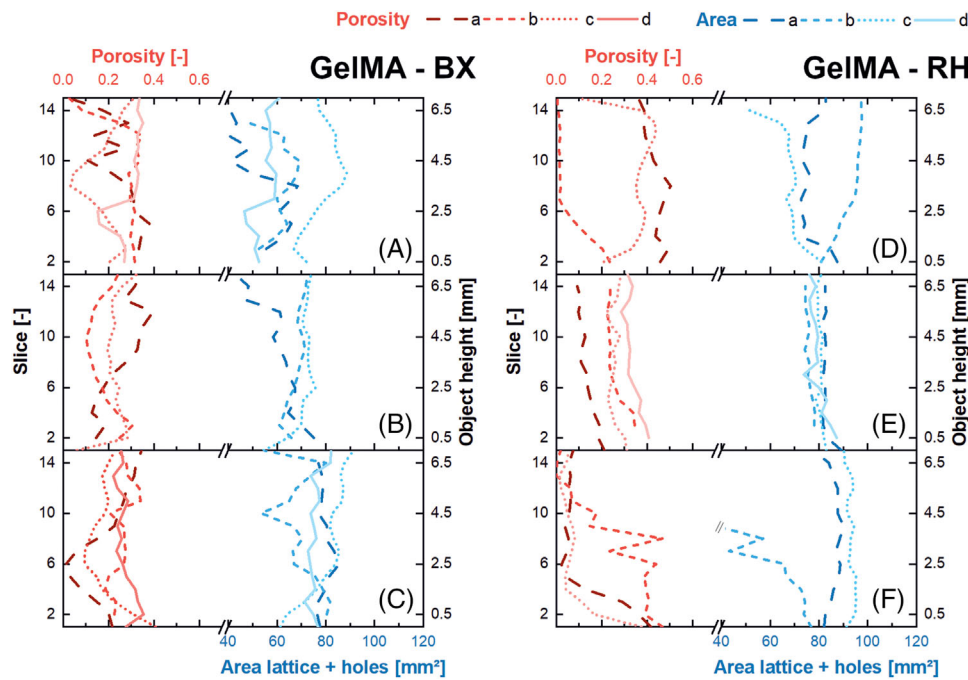


FIGURE 5 Continuation of the area (with enclosed voids) and porosity data against the slice of the 2.5 D MRI data which can be related to a relative object z-height (see also Figure 4). For each ink cartridge, the letters a-b-c-d represent the sequence of the objects extruded ($n_{\text{objects,cartridge}} = 3$ or $n_{\text{objects,cartridge}} = 4$). (A) GelMA ink, BX printer, batch 1, cartridge 1, (B) GelMA, BX, batch 1, cartridge 2, (C) GelMA, BX, batch 1, cartridge 3, (D) GelMA, RH printer, batch 1, cartridge 1, (E) GelMA, RH, batch 1, cartridge 2, (F) GelMA, RH, batch 1, cartridge 3. In (F), the cross-sectional area of object b was lower than 40 mm^2 from slice 9 to the top because of clogging of the nozzle and irregular extrusion. Data was excluded from the analysis.

($n_{\text{objects,printerBX}} = 6$) in comparison to the 3DDiscovery with a mean area porosity of 0.03 ± 0.05 ($n_{\text{objects,printerRH}} = 6$). The mean area porosities of batch 1, 0.02 ± 0.04 ($n_{\text{objects,batch1}} = 6$) and batch 2 with a value of 0.03 ± 0.04 ($n_{\text{objects,batch2}} = 6$) also show deviations. It must be noted that the median porosity of all samples is very small and deviating from the mean porosity due to the skewed pore size distribution with many small and few large holes. Therefore, a much larger number of samples is necessary for statistically significant statements. Additionally, the inspection of the incoming goods might help to set the printing parameters accordingly.

A total number of 21 objects were printed with GelMA ink from one batch ($n_{\text{GelMA ink,batch}} = 1$) using two printers ($n_{\text{printer}} = 2$) and three cartridges of bioink for each printer ($n_{\text{cartridge}} = 3$) with three respectively four objects per cartridge ($n_{\text{GelMA ink,total}} = 2 \times 3 \times (3 \text{ or } 4) = 21$ objects, Figure 5A–F; exemplary slices of one object see Figure S4, Supporting Information). The GelMA area porosity of about 0.2–0.4 is in the same range as in the calciumphosphate scaffolds. Summarizing this data set, there was no pattern recognizable concerning the sequence of the extruded objects within one cartridge and their area or porosity. The covered area of the cross-sections had many nonreproducible deviations between the cartridges for the BioX (Figure 5A–C, mean values between 52.1 and 80.6 mm^2 and ranges from 9.1 to 33.9 mm^2 for the objects). In contrast, the differentiation into homogeneous and irregular objects in terms of their area is more pronounced for the 3DDiscovery (Figure 5D–F, mean values between 65.7 and 93.0 mm^2 and ranges from 4.0 to 51.2 mm^2 (annotation: Figure 5F, object b: only

slices 1–8 were analyzed because of clogging of the nozzle and irregular extrusion). In the 10 samples, the area of two objects strongly deviates from the other eight.

3.3 | Hole area dependence on position within cross-section

The 3D printed cube with its 16 square holes has a uniform design across the xy-cross-section of the object ($n_{\text{slices,object}} = 15$). According to the design, the hole area is expected to be equal within the 16 holes of the xy-cross-section of the object as well as along the z-height. However, experimentally deviations occur: Inner voids tend to have the largest area, as the printhead travels along straight lines to generate the material strands. At edges, the flow of the material may cause inconsistent geometries. Discontinuous strands will create bigger holes if their position is within the scaffold. Defects on the outer walls reduce the total number of the holes of the cross-section. According to this assumption, the holes were grouped for the evaluation of this assumption into the four central holes of the object, the four edge voids and eight holes of the outer ring, that are not positioned at the edges (see Figure 6 and Figure S8, Supporting Information).

Figure 7A depicting the three PLA reference objects shows that the hole area ranges from 2.3 up to 3.0 mm^2 . For all objects, a tendency to a smaller hole size can be seen by ordering the groups to a center/outer/edge hole sequence. While the absolute median value differs

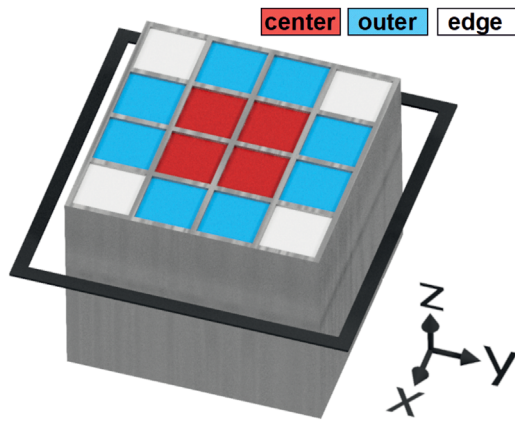


FIGURE 6 Schematic depiction of the hole grouping according to their position within the cross-section. The center of the cross-section consists of four holes (marked in red). At the outer walls of the scaffold, four edge holes (white) and eight outer holes (blue) complete the object.

between objects a, b, and c, this tendency is reproducible. The hole area distribution of the calciumphosphate scaffolds (Figure 7B) is broader and more irregular than the data of the PLA scaffolds. Comparing the sequence from center to edge holes, the inner hole area distribution is narrower than the edge hole distribution with the exception of the outliers. With a broader distribution, a tendency to smaller holes in the “outer holes” and “edge holes” groups was noted, although the medians of the groups do not change by a large absolute value. Additionally, the

differences between the objects a, b, and c blur, which is visually discernible by the overlapping boxes in Figure 7B

The twelve alginate scaffolds (Figure 7C–F) are characterized hole areas smaller than 1.5 mm^2 and some outliers with larger holes sizes, mainly in batch 2 (D,F). While one cartridge (C) was excluded from statistics because of the low number of detected holes, the other three show no clear trend concerning the size of the hole areas within the scaffold and their position. Kruskal–Wallis analysis hinted at a similarity between the outer and edge holes of Figure 7D ($H_{\text{outer}}(2) = 1.31, p = 0.52$; $H_{\text{edge}}(2) = 0.14, p = 0.93$), but the deviations in the distribution of the holes suggest that the value is low for the practical application. The inner holes of the objects a, b, and c ($H_{\text{inner}}(2) = 7.1, p = 0.03$) also differ based on the results of the multicomparison of the (all $p_{\text{multi}} > 0.1$). No significant differences were detected for the objects printed with the 3DDiscovery printer (Figure 7E and F: all $p_{\text{multi}} > 0.24$) except the outer holes of object a and b in E with values of $H_{\text{outer}}(2) = 6.47, p = 0.04$ and a subsequent p_{multi} -value of 0.04 for the respective groups. As the range of the hole size and the sample number of these groups deviated strongly, this should be considered a random occurrence.

The hole size distribution of the GelMA scaffolds (Figure 8) has a wide range. The thickness of GelMA ink strands is sensitive to temperature, which causes deviations. However, structure fidelity is important if the scaffolds inserted into tailor-made cavities or flow-channels.^[39,40] Discontinuous strands that merge up to four or five holes to one of $> 10 \text{ mm}^2$ area as well as temporarily increased flow decreasing the hole size to $< 1 \text{ mm}^2$ were noted. A trend for the extrusion of the objects a, b, c (and d) within a cartridge could be observed for

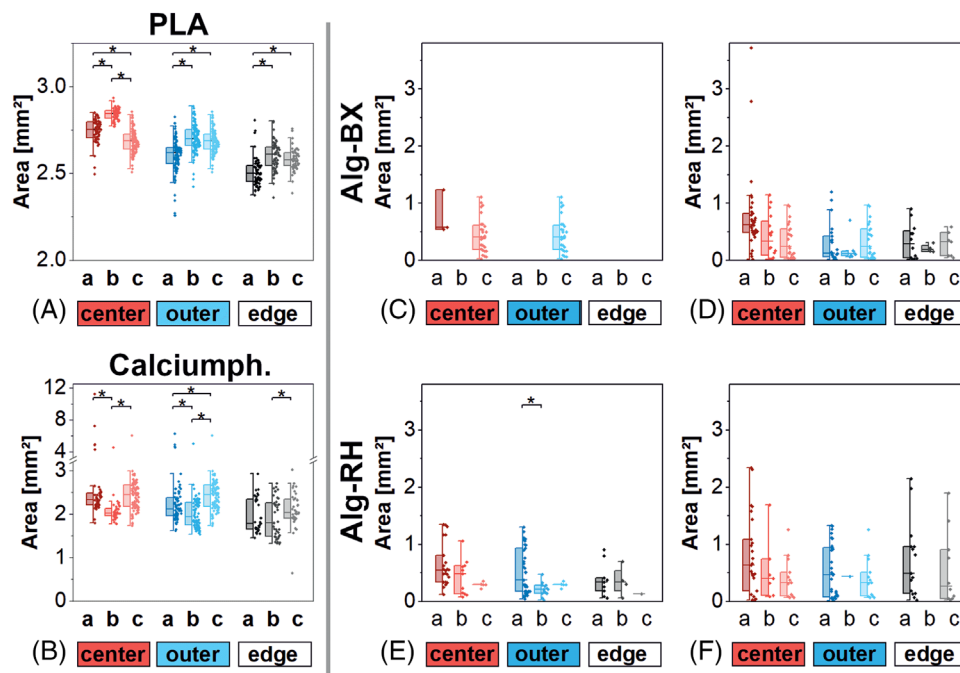


FIGURE 7 Holes sizes of PLA (A), calciumphosphate ink (B) and alginate ink (C–F) scaffolds grouped according to the position of the holes within the cross-section as displayed in Figure 6 and the sequence of the objects a-b-c extruded from one cartridge ($n_{\text{objects,cartridge}} = 3$). Asterisks visualize statistically significant ($p \leq 0.05$) differences between two groups based on the multicomparison test. Specification of the alginate ink scaffolds is as follows: (C) BX printer, batch 1, (D) BX, batch 2, (E) RH printer, batch 1, (F) RH, batch 2.

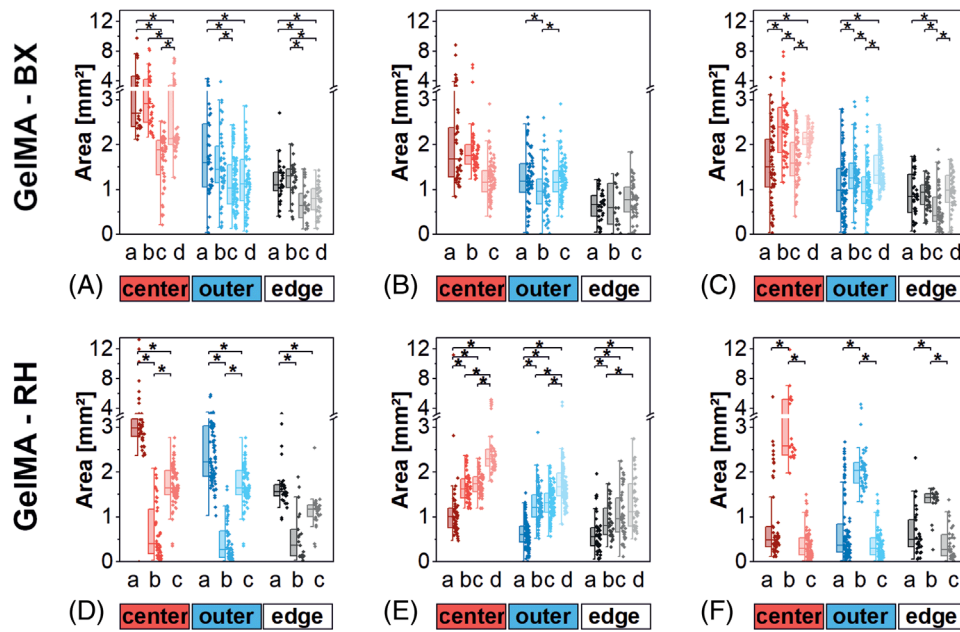


FIGURE 8 Hole sizes of GeIMA scaffolds grouped according to the position of the holes within the cross-section as displayed in Figure 6 and the sequence of the objects a-b-c-d extruded from one cartridge ($n_{\text{objects,cartridge}} = 3$ or $n_{\text{objects,cartridge}} = 4$). Asterisks visualize statistically significant ($p \leq 0.05$) differences between two groups based on the multicomparison test. Specification of the subplots: (A) BX printer, cartridge 1, (B) BX, cartridge 2, (C) BX, cartridge 3, (D) RH, cartridge 1, (E) RH, cartridge 2, (F) RH, cartridge 3.

the BioX printer. With ongoing process time, the hole size decreased in cartridges 1 and 2 (Figure 8A and B). This could be caused by the manual triggering of the cartridge heater and a subsequent heating of the bioink resulting in a lower viscosity and enhanced flow. With the 3DDiscovery, no correlation between the hole area and the extrusion duration occurred. The 18 Kruskal–Wallis tests which compare the center/outer/edge hole size distributions of the six cartridges show significant differences between groups for 16 tests; the two exceptions being the inner and edge holes of Figure 8B ($H_{\text{inner}}(2) = 0.97, p = 0.61$; $H_{\text{edge}}(2) = 1.67, p = 0.43$). The Kruskal–Wallis H values of these 16 tests range from 8.4 to 249.4 and p values from $9.0E-54$ to $1.5E-2$. The respective groups are marked in the figure. Kruskal–Wallis tests were also performed to compare the similarity of the holes within the object. Here only the inner, outer and edge pores of only 1 of the 21 objects did not differ significantly from each other which can maybe be explained by the many outliers within this scaffold (Figure 8F, object a, $H_a(2) = 4.32, p = 0.12$). Online-measurements of the extrusion rate^[41] and technical solutions to control the ambient conditions^[42] might increase the reproducibility.

4 | CONCLUSION

For the robustness of a process, the reproducibility and quality control are key factors. The idea of tailor-made printing with small production units entails the adaption to different printers, material preprocessing or deviations in ambient conditions. Relevant geometric features to describe properties of the printed objects, and therefore critical quality attributes, might be channel diameters, porosity or strand thickness

to describe the diffusion distances as well as deviations from design. Hereby, the geometrical reproducibility of extrusion-based objects manufactured in a layer-by-layer fashion is not directly comparable to other manufacturing techniques. Deviations occur in all spatial directions. Thus, there is a need for three-dimensional control strategies of whole objects.

3D imaging techniques like MRI meet these demands to monitor optically transparent as well as opaque materials in a nondestructive process. Image analysis characterizes patterned structures of 3D printed objects. This study emphasized their intrinsic flexibility and adaptability, as one measurement protocol was able to monitor hydrogel scaffolds of varying water content.

For the statistical analysis of the resulting data, there are two challenges. On the one hand, the desired resolution or quality of the tailor-made objects depends on the application. Commonly used statistics may be classified as “not applicable.” On the other hand, outliers have to be recognized and excluded if necessary. Standardization and system-independent key figures or parameters are desirable, if future developments are to be supported by process simulation.

ACKNOWLEDGMENTS

This work was funded by the German Federal Ministry of Education and Research (BMBF) as project SOP_BioPrint under contract number 13XP5071B. Deutsche Forschungsgemeinschaft is kindly acknowledged for financial support of the instrumental facility Pro²NMR at KIT. The authors would like to thank Henri Müller and Heiko Briesen (both Chair of process systems engineering, TU Munich) for fruitful scientific discussions.

CONFLICT OF INTEREST

The authors declare that they have no known competing financial interests or personal relationships that could have appeared to influence the work reported in this paper.

DATA AVAILABILITY STATEMENT

The data that support the findings of this study are available from the corresponding author, JH, upon reasonable request.

ORCID

Barbara Schmiegel  <https://orcid.org/0000-0003-0234-9110>

REFERENCES

- Gretzinger, S., Beckert, N., Gleadall, A., Lee-Thedieck, C., & Hubbuch, J. (2018). 3D bioprinting – Flow cytometry as analytical strategy for 3D cell structures. *Bioprinting*, 11, e00023.
- Bernhardt, A., Wehrli, M., Paul, B., Hochmuth, T., Schumacher, M., Schuetz, K., & Gelinsky, M. (2015). Improved sterilization of sensitive biomaterials with supercritical carbon dioxide at low temperature. *Plos One*, 10(6), e0129205.
- Cidonio, G., Alcalá-Orozco, C. R., Lim, K. S., Glinka, M., Mutreja, I., Kim, Y.-H., Dawson, J. I., Woodfield, T. B. F., & Oreffo, R. O. C. (2019). Osteogenic and angiogenic tissue formation in high fidelity nanocomposite Laponite-gelatin bioinks. *Biofabrication*, 11(3), 035027. <https://doi.org/10.1088/1758-5090/ab19fd>.
- Di Prima, M., Coburn, J., Hwang, D., Kelly, J., Khairuzzaman, A., & Ricles, L. (2016). Additively manufactured medical products – The FDA perspective. *3D Printing in Medicine*, 2, 1.
- Wehrle, M., Koch, F., Zimmermann, S., Koltay, P., Zengerle, R., Stark, G. B., Strassburg, S., & Finkenzeller, G. (2019). Examination of hydrogels and mesenchymal stem cell sources for bioprinting of artificial osteogenic tissues. *Cellular and Molecular Bioengineering*, 12, 583–597.
- Straub, J. (2015). Initial work on the characterization of additive manufacturing (3D printing) using software image analysis. *Machines*, 3, 55–71.
- Eggert, S., & Huttmacher, D. W. (2019). In vitro disease models 4.0 via automation and high-throughput processing. *Biofabrication*, 11, 43002.
- Radtke, C. P., Hillebrandt, N., & Hubbuch, J. (2018). The Biomaker: An entry-level bioprinting device for biotechnological applications. *Journal of Chemical Technology and Biotechnology*, 93, 792–799. <https://doi.org/10.1002/jctb.5429>.
- Armstrong, A. A., Alleyne, A. G., & Johnson, A. J. W. (2020). 1D and 2D error assessment and correction for extrusion-based bioprinting using process sensing and control strategies. *Biofabrication*, 12, 45023.
- Fahmy, A. R., Becker, T., & Jekle, M. (2020). 3D printing and additive manufacturing of cereal-based materials: Quality analysis of starch-based systems using a camera-based morphological approach. *Innovative Food Science & Emerging Technologies*, 63, 102384.
- Petsiuk, A. L., & Pearce, J. M. (2020). Open source computer vision-based layer-wise 3D printing analysis. *Additive Manufacturing*, 36, 101473.
- Strauß, S., Meutelet, R., Radosevic, L., Gretzinger, S., & Hubbuch, J. (2021). Image analysis as PAT-Tool for use in extrusion-based bioprinting. *Bioprinting*, 21, e00112.
- Alonzo, M., Dominguez, E., Alvarez-Primo, F., Quinonez, A., Munoz, E., Puebla, J., Barron, A., Aguirre, L., Vargas, A., Ramirez, J. M., & Joddar, B. (2020). A comparative study in the printability of a bioink and 3D models across two bioprinting platforms. *Materials Letters*, 264, 127382.
- Ribeiro, A., Blokzijl, M. M., Levato, R., Visser, C. W., Castilho, M., Hennink, W. E., Vermonden, T., & Malda, J. (2018). Assessing bioink shape fidelity to aid material development in 3D bioprinting. *Biofabrication*, 10(1), 014102.
- Wang, L., Xu, M., Zhang, L., Zhou, Q., & Luo, L. (2016). Automated quantitative assessment of three-dimensional bioprinted hydrogel scaffolds using optical coherence tomography. *Biomedical Optics Express*, 7(3), 894–910. <https://doi.org/10.1364/BOE.7.000894>.
- Cahuana-Bartra, P., Cahuana-Cárdenas, A., Brunet-Llobet, L., et al. (2020). The use of 3D additive manufacturing technology in autogenous dental transplantation. *3D Printing in Medicine*, 6, 16. <https://doi.org/10.1186/s41205-020-00070-9>.
- Filippou, V., & Tsoumpas, C. (2018). Recent advances on the development of phantoms using 3D printing for imaging with CT, MRI, PET, SPECT, and ultrasound. *Medical Physics*, 45, e740–e760.
- Wiese, M., Benders, S., Blümich, B., & Wessling, M. (2018). 3D MRI velocimetry of non-transparent 3D-printed staggered herringbone mixers. *Chemical Engineering Journal*, 343, 54–60.
- Flood, P., Page, H., Reynaud, E. G. (2016). Using hydrogels in microscopy: A tutorial. *Micron*, 86, 7–16. <https://doi.org/10.1016/j.micron.2016.02.002>.
- Chimene, D., Kaunas, R., & Gaharwar, A. K. (2020). Hydrogel bioink reinforcement for additive manufacturing: A focused review of emerging strategies. *Advanced Materials*, 32.
- Wenger, L., Radtke, C. P., Goepper, J., Woerner, M., & Hubbuch, J. (2020). 3D-printable and enzymatically active composite materials based on hydrogel-filled high internal phase emulsions. *Frontiers in Bioengineering and Biotechnology*, 8, 713. <https://doi.org/10.3389/fbioe.2020.00713>.
- Han, B., Yun, G. Y., Boley, J. W., Kim, S. H., Hwang, J. Y., & Chiu, G. T.-C., & Park, K. (2016). Dropwise gelation-dehydration kinetics during drop-on-demand printing of hydrogel-based materials. *International Journal of Heat & Mass Transfer*, 97, 15–25.
- Tummala, G. K., Felde, N., Gustafsson, S., Bubholz, A., Schoeder, S., & Mhrranyan, A. (2017). Light scattering in poly(vinyl alcohol) hydrogels reinforced with nanocellulose for ophthalmic use. *Optical Materials Express*, 7(8), 2824–2837. <https://doi.org/10.1364/OME.7.002824>.
- Teo, M. Y., Kee, S., RaviChandran, N., Stuart, L., Aw, K. C., & Stringer, J. (2020). Enabling Free-Standing 3D Hydrogel Microstructures with Microreactive Inkjet Printing. *ACS applied materials & interfaces*, 12, 1832–1839.
- Arndt, F., Schuhmann, S., Guthausen, G., Schuetz, S., & Nirschl, H. (2017). In situ MRI of alginate fouling and flow in ceramic hollow fiber membranes. *Journal of Membrane Science*, 524, 691–699. <https://doi.org/10.1016/j.memsci.2016.11.079>.
- Bastawrous, S., Wake, N., Levin, D., & Ripley, B. (2018). Principles of three-dimensional printing and clinical applications within the abdomen and pelvis. *Abdominal Radiology (New York)*, 43, 2809–2822.
- Busato, A., Fumene Feruglio, P., Parnigotto, P. P., Marzola, P., & Sbarbati, A. (2016). In vivo imaging techniques: A new era for histochemical analysis. *European Journal of Histochemistry*, 60, 273–279.
- Estelrich, J., Sanchez-Martin, M. J., & Busquets, M. A. (2015). Nanoparticles in magnetic resonance imaging: From simple to dual contrast agents. *International Journal of Nanomedicine*, 10, 1727–1741.
- Tondera, C., Hauser, S., Krüger-Genge, A., Jung, F., Neffe, A. T., Lendlein, A., Klopffleisch, R., Steinbach, J., Neuber, C., & Pietzsch, J. (2016). Gelatin-based hydrogel degradation and tissue interaction in vivo: Insights from multimodal preclinical imaging in immunocompetent nude mice. *Theranostics*, 6, 2114–2128.
- Mancha Sánchez, E., Gómez-Blanco, J. C., López Nieto, E., Casado, J. G., Macías-García, A., Díaz Diez, M. A., Carrasco-Amador, J. P., Torrejón Martín, D., Sánchez-Margallo, F. M., & Pagador, J. B. (2020). Hydrogels for bioprinting: A systematic review of hydrogels synthesis, bioprinting parameters, and bioprinted structures behavior. *Frontiers in Bioengineering and Biotechnology*, 8, 776.
- Mandrycky, C., Wang, Z., Kim, K., & Kim, D.-H. (2016). 3D bioprinting for engineering complex tissues. *Biotechnology Advances*, 34, 422–434.

32. Otsu, N. (1979). A threshold selection method from gray-level histograms. *IEEE Transactions on Systems, Man, and Cybernetics*, *9*, 62–66.
33. Janmaleki, M., Liu, J., Kamkar, M., Azarmanesh, M., Sundararaj, U., & Nezhad, A. S. (2021). Role of temperature on bio-printability of gelatin methacryloyl bioink in two-step cross-linking strategy for tissue engineering applications. *Biomedical Materials*, *16*, 015021. <https://doi.org/10.1088/1748-605X/abbcc9>.
34. Ottone, M. L., Peirotti, M. B., & Deiber, J. A. (2009). Rheokinetic model to characterize the maturation process of gelatin solutions under shear flow. *Food Hydrocolloids*, *23*, 1342–1350.
35. Ruiz-Cantu, L., Gleadall, A., Faris, C., Segal, J., Shakesheff, K., & Yang, J. (2020). Multi-material 3D bioprinting of porous constructs for cartilage regeneration. *Materials science & engineering. C, Materials for biological applications*, *109*, 110578.
36. Schmieg, B., Nguyen, M., & Franzreb, M. (2020). Simulative minimization of mass transfer limitations within hydrogel-based 3D-printed enzyme carriers. *Frontiers in Bioengineering and Biotechnology*, *8*, 365.
37. Xu, Y., & Wang, X. (2015). Fluid and cell behaviors along a 3D printed alginate/gelatin/fibrin channel. *Biotechnology and Bioengineering*, *112*, 1683–1695.
38. Schmieder, S., Barthel, L., Mueller, H., Meyer, V., & Briesen, H. (2019). From three-dimensional morphology to effective diffusivity in filamentous fungal pellets. *Biotechnology and Bioengineering*, *116*, 3360–3371.
39. Maier, M., Radtke, C. P., Hubbuch, J., Niemeyer, C. M., & Rabe, K. S. (2018). On-demand production of flow-reactor cartridges by 3D printing of thermostable enzymes. *Angewandte Chemie International Edition*, *57*, 5539–5543.
40. Schmieg, B., Doebber, J., Kirschhoefer, F., Pohl, M., & Franzreb, M. (2019). Advantages of hydrogel-based 3D-printed enzyme reactors and their limitations for biocatalysis. *Frontiers in Bioengineering and Biotechnology*, *6*, 211. <https://doi.org/10.3389/fbioe.2018.00211>.
41. Fisch, P., Holub, M., & Zenobi-Wong, M. (2021). Improved accuracy and precision of bioprinting through progressive cavity pump-controlled extrusion. *Biofabrication*, *13*, 15012.
42. Matamoros, M., Gómez-Blanco, J. C., Sánchez, Á. J., Mancha, E., Marcos, A. C., Carrasco-Amador, J. P., & Pagador, J. B. (2020). Temperature and humidity PID controller for a bioprinter atmospheric enclosure system. *Micromachines*, *11*, 999.

SUPPORTING INFORMATION

Additional supporting information may be found in the online version of the article at the publisher's website.

How to cite this article: Schmieg, B., Gretzinger, S., Schuhmann, S., Guthausen, G., & Hubbuch, J. (2022). Magnetic Resonance Imaging as a tool for quality control in extrusion-based bioprinting. *Biotechnology Journal*, e2100336. <https://doi.org/10.1002/biot.202100336>